Spin correlations of quantum spin liquid and quadrupole-ordered states of $Tb_{2+x}Ti_{2-x}O_{7+y}$

Hiroaki Kadowaki,[1] Mika Wakita,[1] Björn Fåk,[2] Jacques Ollivier,[2] Seiko Ohira-Kawamura,[3] Kenji Nakajima,[3] and Jeffrey W. Lynn[4]

[1]*Department of Physics, Tokyo Metropolitan University, Hachioji, Tokyo 192-0397, Japan*

[2]*Institut Laue-Langevin, CS 20156, 38042 Grenoble Cedex 9, France*

[3]*Neutron Science Section, MLF, J-PARC Center, Shirakata, Tokai, Ibaraki 319-1195, Japan*

[4]*NIST Center for Neutron Research, National Institute of Standards and Technology, Gaithersburg, Maryland 20899-6102, USA*

(Received 2 September 2018; revised manuscript received 7 November 2018; published 7 January 2019)

Spin correlations of the frustrated pyrochlore oxide $Tb_{2+x}Ti_{2-x}O_{7+y}$ have been investigated by using inelastic neutron scattering on single-crystalline samples ($x = -0.007, 0.000$, and 0.003), which have the putative quantum-spin-liquid (QSL) or electric-quadrupolar ground states. Spin correlations, which are notably observed in nominally elastic scattering, show short-range correlations around L points [$\boldsymbol{q} = (\frac{1}{2}, \frac{1}{2}, \frac{1}{2})$], tiny antiferromagnetic Bragg scattering at L and Γ points, and pinch-point-type structures around Γ points. The short-range spin correlations were analyzed using a random-phase approximation (RPA) assuming the paramagnetic state and two-spin interactions among Ising spins. These analyses have shown that the RPA scattering intensity well reproduces the experimental data using temperature- and x-dependent coupling constants of up to tenth-neighbor site pairs. This suggests that no symmetry breaking occurs in the QSL sample and that a quantum treatment beyond the semiclassical RPA approach is required. Implications of the experimental data and the RPA analyses are discussed.

DOI: 10.1103/PhysRevB.99.014406

I. INTRODUCTION

Geometrically frustrated magnets archetypally on the two-dimensional (2D) triangle [1] and kagome [2,3] lattices and on the three-dimensional (3D) pyrochlore lattice [4] have been actively studied for decades [5]. Among classical frustrated magnets, spin ice [6] has been extensively studied from many viewpoints, e.g., macroscopically degenerate ground states [7], partial lifting of the degeneracy under magnetic field [8], and fractionalized excitations [9,10]. Quantum effects in frustrated magnetic systems ranging from quantum annealing [11,12] to quantum-spin-liquid (QSL) states [13], the origin of which dates back to the proposal of the resonating valence bond state [14], have attracted much attention. Experimental challenges of finding real QSL substances [15,16] and of investigating QSL states using available techniques [17–22] have been addressed in recent years.

Among frustrated magnetic pyrochlore oxides [4] a non-Kramers pyrochlore magnet $Tb_{2+x}Ti_{2-x}O_{7+y}$ (TTO) [23] has been investigated for decades as a QSL candidate since conventional magnetic order has not been observed in any experiments under zero field and zero static pressure [4,16]. On the basis of theoretical insight that TTO is not much different from classical spin ice, the phrase quantum spin ice (QSI) was coined for the QSL state of TTO [24,25]. However, its nature has remained elusive. Recently, we showed that this putative QSL state is limited in a range of the small off-stoichiometry parameter $x < x_c \simeq -0.0025$ [23,26,27]. In the other range $x_c < x$, we showed that TTO undergoes a phase transition most likely to an electric multipolar [or quadrupole-ordered (QO)] state ($T < T_c$) [28–30], which is described by a pseudospin-$\frac{1}{2}$ Hamiltonian modified from the classical spin ice to a quantum model by adding transverse pseudospin terms [31]. The estimated parameter set of this Hamiltonian [28] is close to the theoretical phase boundary between the electric quadrupolar state and a U(1) QSL state (QSI) [32,33], which is thereby a theoretical QSL candidate for TTO. At present, few researchers have addressed the problem of the QSL state of TTO using well-x-controlled samples.

Previous neutron scattering experiments on TTO, which were performed on samples with unknown and known x, showed that spin correlations, defined by the wave vector dependence of scattering intensity, are most clearly seen in energy-resolution-limited (nominally) elastic scattering at low temperatures. In the observed spin correlations there are three important features: magnetic short-range order (SRO) with the wave vector $\boldsymbol{q} = (\frac{1}{2}, \frac{1}{2}, \frac{1}{2})$ (L point of the first Brillouin zone of the fcc lattice) [34–37], pinch-point structures around $\boldsymbol{q} = 0$ (Γ point) [35,36], and tiny antiferromagnetic Bragg reflections at the L and Γ points [26,28]. It should be noted that the details of the observed scattering intensities in these studies depended on samples (on x). This may intriguingly suggest that the ground states of TTO are potentially highly degenerate and they are lifted in various ways depending on slight differences in samples.

Very recently, we performed inelastic neutron scattering (INS) experiments on x-controlled TTO single-crystalline samples with $x = -0.007 < x_c$ (QSL) and $x_c < x = 0.000, 0.003$ (QO) [23]. In this paper we focus on the $\boldsymbol{q} = (\frac{1}{2}, \frac{1}{2}, \frac{1}{2})$ SRO of these samples and perform quantitative analyses in order to shed light on how these spin correlations reflect the QSL state. In previous investigations [37,38], analyses of the $\boldsymbol{q} = (\frac{1}{2}, \frac{1}{2}, \frac{1}{2})$ SRO were carried out by assuming

that there exist static short-range classical spins with cluster sizes of the order of 10 Å. However, no clusters which adequately reproduce the observed intensity pattern were found, although a few clusters showing limited goodness of fit were obtained [37,38]. This failure indicates either that the samples were not well controlled or that the analysis methods they used are not sufficiently systematic.

The first problem of controlling the composition of the samples is resolved in the present study. In contrast, the second problem can originate from a profound property of the QSL state and will be resolved only by analyses reflecting the quantum nature of the many-body ground state. However, since no practical quantum model calculations are available at present, in the present study, we attempt to apply a systematic but still semiclassical approach using a random-phase approximation (RPA) [39]. This would lead us to a reasonable result if the SRO could be interpreted within the classical spin paradigm or would lead us to a certain paradoxical result if it essentially contains many-body quantum effects.

II. METHODS

A. Experimental methods

Single-crystalline samples of $Tb_{2+x}Ti_{2-x}O_{7+y}$ with $x = -0.007, 0.000$, and 0.003 used in this study are those of Ref. [23], where methods of the sample preparation and the estimation of x are described. The QSL sample with $x = -0.007$ remains in the paramagnetic state down to 0.1 K. The QO samples with $x = 0.000$ and $x = 0.003$ very likely have small and large electric quadrupole orders, respectively, at $T \ll T_c \sim 0.4$ K [26,27]. We note that the values of x among different investigation groups are not necessarily consistent [23] and that our x values of the samples used in Refs. [23,26–29,40,41] are self-consistent.

Neutron scattering experiments were carried out on the time-of-flight (TOF) spectrometer IN5 [42,43] operated with $\lambda = 8$ Å at the Institut Laue-Langevin (ILL) for the $x = -0.007$ and 0.000 crystal samples. The energy resolution of this condition was $\Delta E = 0.021$ meV (FWHM) at the elastic position. Neutron scattering experiments for the $x = 0.003$ crystal sample were performed on the TOF spectrometer AMATERAS operated with $\lambda = 7$ Å at the Japan Proton Accelerator Research Complex (J-PARC). The energy resolution of this condition was $\Delta E = 0.024$ meV (FWHM) at the elastic position. Each crystal sample was mounted in a dilution refrigerator to make its (h, h, l) plane coincide with the horizontal scattering plane of the spectrometer. The observed intensity data were corrected for background and absorption using a homemade program [44]. Construction of a four-dimensional $S(\boldsymbol{Q}, E)$ data object from a set of the TOF data taken by rotating each crystal sample was performed using HORACE [45].

To analyze the $\boldsymbol{Q}$ dependence of the (nominally) elastic scattering intensity (Fig. 1 in Ref. [23]), we integrated $S(\boldsymbol{Q}, E)$ in a small energy range $-\epsilon < E < \epsilon$. We chose $\epsilon = 0.025$ and 0.030 meV for IN5 and AMATERAS data, respectively, which are a little larger than the instrumental resolutions. These 3D data sets $[S(\boldsymbol{Q})]_{\rm el} = \int_{-\epsilon}^{\epsilon} S(\boldsymbol{Q}, E) dE$ are normalized by the method described in Ref. [23], i.e., using the "arb. units" of Fig. 1 in Ref. [23]. Consequently, the elastic intensities can be compared mutually among the three samples.

B. RPA model calculation

The RPA model calculation of $S(\boldsymbol{Q}, E)$ using the pseudospin-$\frac{1}{2}$ Hamiltonian appropriate for quadrupole-ordered phases is described in Ref. [40]. We used a similar RPA method to calculate the elastic scattering intensity $[S(\boldsymbol{Q})]_{\rm el}$ assuming that the system is in the paramagnetic phase. This assumption is made because we are interested mainly in the low-temperature QSL and the high-temperature paramagnetic states. Details and related definitions are described in Appendix A.

For the sake of simplicity we consider a pseudospin-$\frac{1}{2}$ Hamiltonian which is decoupled between magnetic dipole ($\sigma_{\boldsymbol{r}}^z$) and electric quadrupole ($\sigma_{\boldsymbol{r}}^x$ and $\sigma_{\boldsymbol{r}}^y$) terms, the latter of which can be neglected for the present purpose. We adopt a magnetic Hamiltonian expressed by

$$H_{\rm m} = \sum_m J_m \left\{ \sum_{\langle \boldsymbol{r}, \boldsymbol{r}' \rangle_m} \sigma_{\boldsymbol{r}}^z \sigma_{\boldsymbol{r}'}^z \right\} + D r_{\rm nn}^3 \times \sum_{\langle \boldsymbol{r}, \boldsymbol{r}' \rangle} \left\{ \frac{z_{\boldsymbol{r}} \cdot z_{\boldsymbol{r}'}}{|\Delta \boldsymbol{r}|^3} - \frac{3[z_{\boldsymbol{r}} \cdot \Delta \boldsymbol{r}][z_{\boldsymbol{r}'} \cdot \Delta \boldsymbol{r}]}{|\Delta \boldsymbol{r}|^5} \right\} \sigma_{\boldsymbol{r}}^z \sigma_{\boldsymbol{r}'}^z, \quad (1)$$

which is an expansion of that of Refs. [28,40]. The first term in Eq. (1) stands for magnetic coupling allowed by the space group symmetry between the Ising spin operators. The summation runs over coupling constants J_m ($m = 1, \ldots, m_{\rm max}$, $m_{\rm max} \leqslant 16$) and corresponding site pairs $\langle \boldsymbol{r}, \boldsymbol{r}' \rangle_m$. These site pairs are listed in Table III in Appendix A. The nearest-neighbor (NN) coupling constant J_1 is usually expressed as $J_{\rm nn}$ for the NN spin ice model ($J_{\rm nn} = J_1 > 0$). The other couplings as far as tenth-neighbor site pairs had to be included to obtain a good fit of the experimental data. Since the coupling constants beyond third-neighbor site pairs ($J_{m>4}$) are probably much smaller than J_1, they would be effective values or experimental parameters. The second term in Eq. (1) represents the classical dipolar interaction [46], where $r_{\rm nn}$ is the NN distance and $\Delta \boldsymbol{r} = \boldsymbol{r} - \boldsymbol{r}'$. The parameter D is determined by the magnitude of the magnetic moment of the crystal-field ground-state doublet. We adopt $D = 0.29$ K, corresponding to the magnetic moment $4.6 \mu_{\rm B}$ [28].

The generalized susceptibility $\chi_{\nu,\nu'}(\boldsymbol{k}, E = 0)$ is computed by solving Eq. (A1) with $E = 0$, i.e.,

$$\sum_{\nu''} [\delta_{\nu,\nu''} - \chi_{\rm L} J_{\nu,\nu''}(\boldsymbol{k})] \chi_{\nu'',\nu'}(\boldsymbol{k}, 0) = \delta_{\nu,\nu'} \chi_{\rm L}, \quad (2)$$

where $J_{\nu,\nu'}(\boldsymbol{k})$ denotes the Fourier transform of the magnetic coupling constants [Eq. (A2)] and $\chi_{\rm L}$ is the local susceptibility [Eq. (A3)]. Using $\chi_{\nu,\nu'}(\boldsymbol{k}, 0)$, the elastic scattering $[S(\boldsymbol{Q})]_{\rm el}$ is given by

$$[S(\boldsymbol{Q} = \boldsymbol{G} + \boldsymbol{k})]_{\rm el} \propto f(Q)^2 \sum_{\rho,\sigma,\nu,\nu'} (\delta_{\rho,\sigma} - \hat{Q}_\rho \hat{Q}_\sigma) \times U_{\rho,z}^{(\nu)} U_{\sigma,z}^{(\nu')} \chi_{\nu,\nu'}(\boldsymbol{k}, 0) \cos[\boldsymbol{G} \cdot (\boldsymbol{d}_\nu - \boldsymbol{d}_{\nu'})], \quad (3)$$

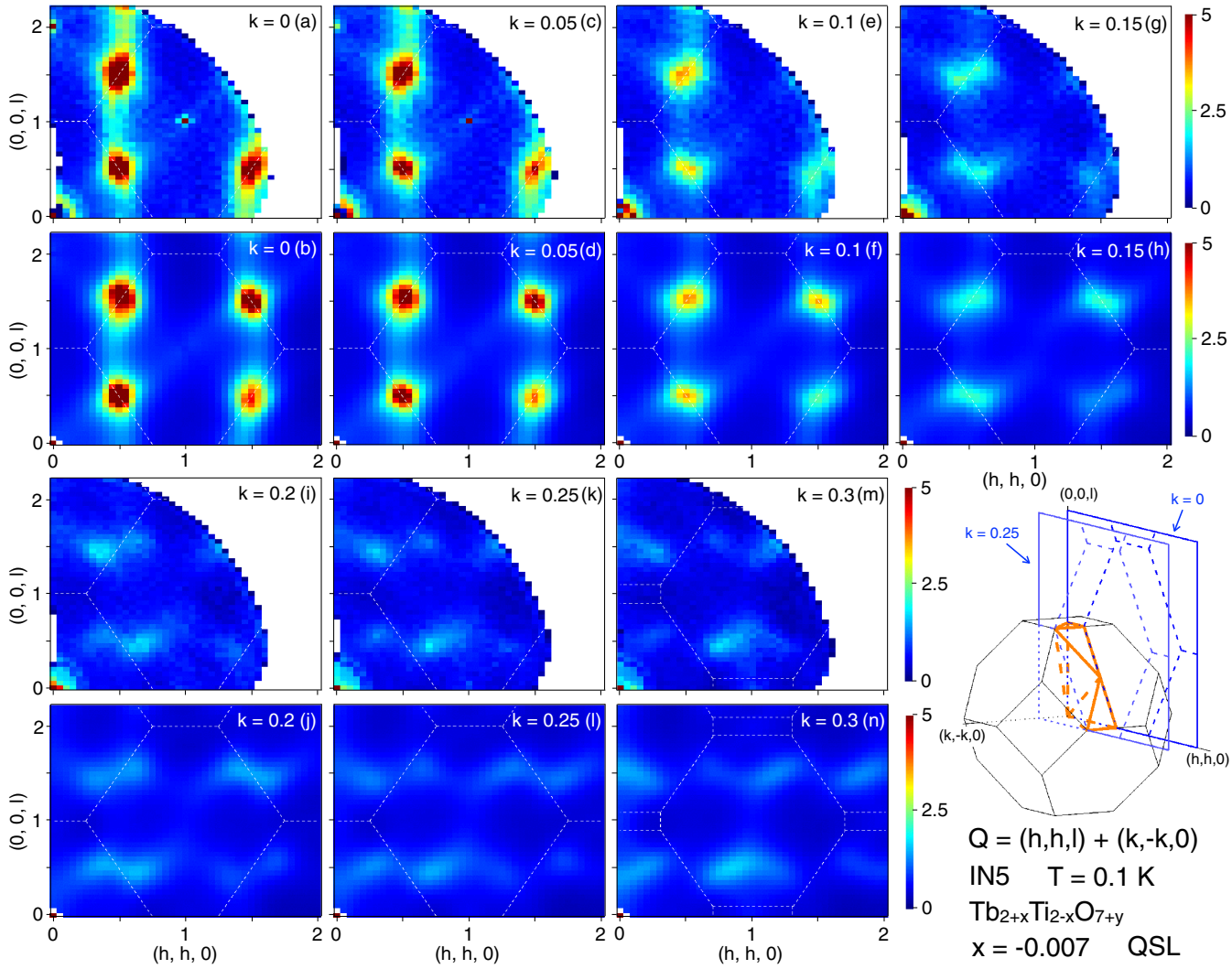

FIG. 1. Intensity maps of 3D data $[S(\boldsymbol{Q})]_{\rm el}$ taken at 0.1 K for the QSL sample with $x = -0.007$. The 3D data are viewed by (a), (c), (e), (g), (i), (k), and (m) 2D slices, which are parallel cross sections of $\boldsymbol{Q} = (h, h, l) + (k, -k, 0)$ with fixed k. These can be compared to (b), (d), (f), (h), (j), (l), and (n) the typical RPA $[S(\boldsymbol{Q})]_{\rm el}$ obtained by least-squares fit using the 13 coupling constants, $J_1, \ldots, J_{13}$, listed in Table I. Dashed lines in these 2D slices in (a)–(n) are boundaries of Brillouin zones. The bottom right corner shows the first Brillouin zone of the fcc lattice (thin black lines), irreducible zone (thick orange lines), and two 2D slice planes labeled $k = 0$ and 0.25 (blue lines).

where $f(Q)$ is the form factor of Tb^{3+} in the quasielastic approximation [Eq. (A5)].

III. RESULTS

A. QSL sample with $x = -0.007$

Figures 1(a), 1(c) 1(e), 1(g), 1(i), 1(k), and 1(m) show a 3D data set $[S(\boldsymbol{Q})]_{\rm el}$ taken at 0.1 K for the QSL sample with $x = -0.007$. These 3D data are shown by seven 2D slices of $\boldsymbol{Q} = (h, h, l) + (k, -k, 0)$ with fixed k values. Two slice planes with $k = 0$ and 0.25 are illustrated in the bottom right corner of Fig. 1 with the first Brillouin zone of the fcc lattice and an irreducible zone. From Fig. 1 one can see that the observed $\boldsymbol{Q}$ range encompasses an independent part of the first Brillouin zone, which is an advantage over the previous experiments, which is limited to the 2D slice with $k = 0$ [34–37].

The observed 3D data $[S(\boldsymbol{Q})]_{\rm el}$ in Fig. 1 show two features: strong short-range spin correlations with wave vector $\boldsymbol{q} = (\frac{1}{2}, \frac{1}{2}, \frac{1}{2})$ and very weak pinch-point structures around $\boldsymbol{Q} = (1, 1, 1)$ and (0,0,2). By comparing the 2D slice in Fig. 1(a) with those of previous investigations [34–37], one can see both differences and similarities among the investigations. This fact confirms the importance of controlling the x value for quantitative studies.

In order to measure the temperature dependence of the $\boldsymbol{q} = (\frac{1}{2}, \frac{1}{2}, \frac{1}{2})$ SRO we measured intensities along a trajectory through $\boldsymbol{Q} = (\frac{1}{2}, \frac{1}{2}, \frac{1}{2})$ by fixing the sample rotation angle. The resulting temperature dependence of $[S(\boldsymbol{Q})]_{\rm el}$ is plotted in Fig. 2. As temperature is decreased below 0.4 K, the spin correlations grow continuously without a phase transition. We estimate the correlation length ξ from the half width at half maximum (HWHM) of the peak ($1/\xi$ = HWHM). It increases to $\xi \sim 20$ Å at 0.1 K. This correlation length and the temperature scale of 0.4 K agree with those reported in Ref. [38],

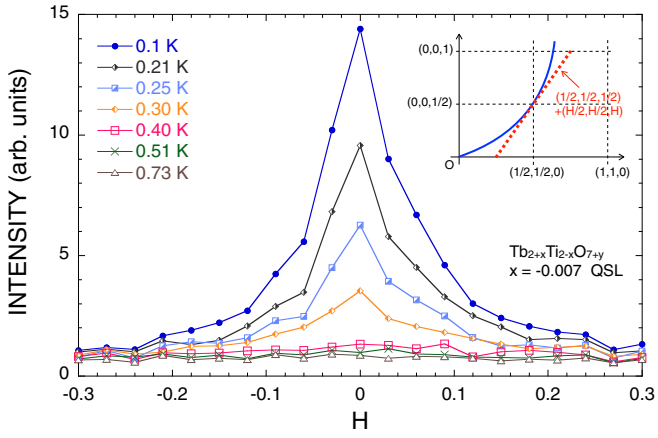

FIG. 2. Temperature dependence of intensity $[S(\boldsymbol{Q})]_{\rm el}$ along a trajectory through $\boldsymbol{Q} = (\frac{1}{2}, \frac{1}{2}, \frac{1}{2})$, which was measured by fixing the sample rotation angle. The abscissa is a projection of the $\boldsymbol{Q}$ trajectory (blue line in inset) to a straight line $\boldsymbol{Q} = (1/2, 1/2, 1/2) + (H/2, H/2, H)$ (red dashed line in inset).

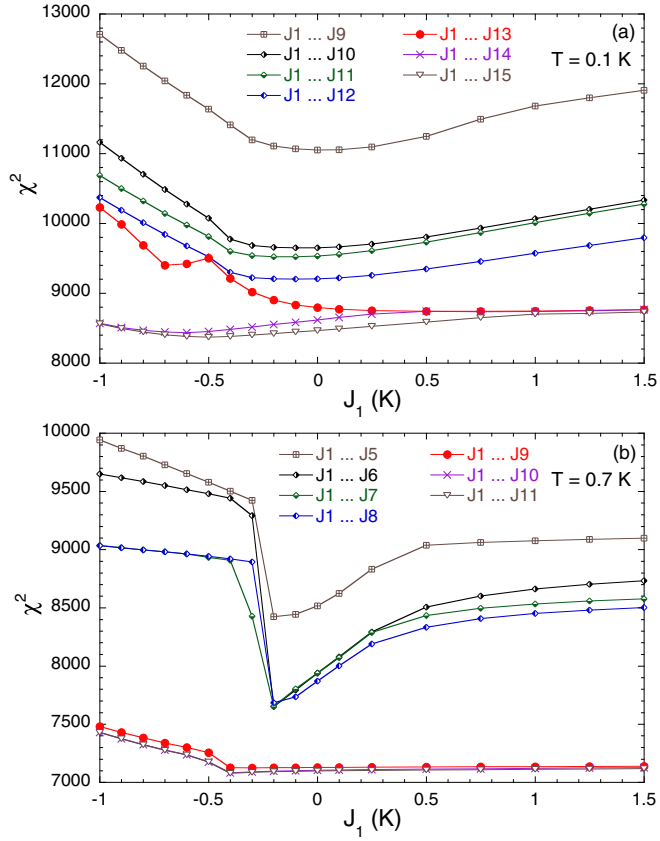

FIG. 3. Minimized values of the weighted sum of squared residuals χ^2 as a function of the fixed parameter J_1. (a) Results of least-squares fits of $[S(\boldsymbol{Q})]_{\rm el}$ with adjustable parameters J_m ($m \leqslant m_{\rm max} = 9, \ldots, 15$) for the QSL sample with $x = -0.007$ taken at 0.1 K (Fig. 1). The number of fit data is 10 185. (b) Results of least-squares fits of $[S(\boldsymbol{Q})]_{\rm el}$ with adjustable parameters J_m ($m \leqslant m_{\rm max} = 5, \ldots, 11$) for the QSL sample with $x = -0.007$ taken at 0.7 K (Fig. 4). The number of fit data is 10 147.

where powder samples were used (Fig. 3(b) in Ref. [38]). We note that the correlation length reported in Ref. [37], where a single crystal sample was used, is significantly shorter (∼8 Å).

An important point concerning the discrepancy of the correlation length noted above concerns the thermal response time of the system. In particular, we observed very slow cooling of the sample especially below 0.4 K in the present experimental condition. More specifically, it took about 2 days for the scattering intensity to become time independent after cooling the mixing chamber down to 0.1 K. This slow cooling is ascribable to very low thermal conductivity of TTO [48] and the large size of the crystal sample for INS. One has to carefully distinguish this long relaxation time from other interpretations, for example, the cooling protocol dependence reported in Ref. [49], where the authors might not have waited enough time, which may possibly result in a short correlation length.

We performed least-squares fits of the observed 3D data set $[S(\boldsymbol{Q})]_{\rm el}$ to the RPA intensity [Eq. (3)]. Adjustable parameters are the coupling constants J_m ($1 \leqslant m \leqslant m_{\rm max}$), the local susceptibility $\chi_{\rm L}$, and an intensity scale factor. After several trial computations, we became aware of the problem that these parameters cannot be independently adjusted. To avoid this problem and exclude unrealistic solutions, we fixed J_1 and imposed a restriction on J_m ($2 \leqslant m \leqslant m_{\rm max}$) by adding the penalty function $\sum_{2\leqslant m\leqslant m_{\rm max}} (\frac{J_m}{1\,\rm K})^8$ to the weighted sum of squared residuals

$$\chi^2 = \sum_{i=1}^{N} \left(\frac{\mathrm{obs}(i) - \mathrm{calc}(i)}{\mathrm{error}(i)} \right)^2, \qquad (4)$$

where $N = 10\,185$ is the number of intensity data used in the fitting. Technical details of the least-squares fits are discussed in Appendix B and Ref. [47].

In Fig. 3(a) we plot minimized values of χ^2 as a function of fixed J_1 (a detailed discussion of inspecting the least-squares fits is given in Ref. [47]). As J_1 is decreased in the range $J_1 < -5D/3$, which favors the antiferromagnetic "all-in–all-out" long-range order (LRO) for $J_{m>1} = 0$ [46], the fits become unsatisfactory. These plots also show that the inclusion of further coupling constants J_m with $m_{\rm max} \geqslant 14$ does not improve the fitting.

By inspecting 3D data $[S(\boldsymbol{Q})]_{\rm el}$ calculated using several sets of fitted parameters, we chose a typical good result of the fitting. This typical $[S(\boldsymbol{Q})]_{\rm el}$ is shown in Figs. 1(b), 1(d) 1(f), 1(h), 1(j), 1(l), and 1(n), which is calculated using the values of $J_1, \ldots, J_{13}$ listed in Table I. One can see that the RPA model calculation excellently reproduces the observed $[S(\boldsymbol{Q})]_{\rm el}$. Almost the same features of the $\boldsymbol{q} = (\frac{1}{2}, \frac{1}{2}, \frac{1}{2})$ SRO, the very weak pinch-point structures, and the other structures in $\boldsymbol{Q}$ space are seen in both the observed and calculated $[S(\boldsymbol{Q})]_{\rm el}$. This goodness of fit indicates that the QSL sample retains the space group symmetry of the pyrochlore structure ($Fd\bar{3}m$) as low as 0.1 K. The coupling constants listed in Table I are much larger than those expected for bare exchange interactions; for example, the seventh-neighbor coupling J_9 is as large as the nearest-neighbor J_1. This fact indicates either that the coupling constants are strongly renormalized, e.g., by

TABLE I. Typical coupling constants J_m (in units of K) of Eq. (1) obtained by least-squares fits of observed 3D data sets $[S(\boldsymbol{Q})]_{\rm el}$ to Eq. (3). The calculated $[S(\boldsymbol{Q})]_{\rm el}$ using these J_m are shown in Fig. 1 ($x = -0.007$, $T = 0.1$ K), Fig. 4 ($x = -0.007$, $T = 0.7$ K), Fig. 5 ($x = 0.000$, $T = 0.1$ K), Fig. 6 ($x = 0.000$, $T = 0.7$ K), and Fig. 8 ($x = 0.003$, $T = 0.1$ K). Numerical uncertainty of J_m is discussed in Appendix B and Ref. [47].

3D data	J_1	J_2	J_3	J_4	J_5	J_6	J_7	J_8	J_9	J_{10}	J_{11}	J_{12}	J_{13}	J_{14}
Fig. 1	1.0	0.824	1.011	0.176	0.184	0.410	0.436	0.355	1.060	−0.026	−0.066	−0.071	0.378	
Fig. 4	1.0	0.070	0.536	−0.373	−0.370	0.076	−0.007	−0.020	0.919					
Fig. 5	1.0	0.836	1.191	0.102	0.109	0.487	0.745	0.574	1.732	0.037	0.014	−0.137	0.464	
Fig. 6	1.0	−0.101	0.751	−0.501	−0.408	0.191	0.078	−0.019	1.364					
Fig. 8	0.25	−0.279	−0.040	−0.237	−0.081	−0.124	0.297	0.022	0.098	−0.061	−0.031	−0.060	−0.119	0.191

integrating out excited states with $E > \epsilon$, or that the present analysis is an experimental parametrization.

Figures 4(a), 4(c) 4(e), 4(g), 4(i), 4(k), and 4(m) show a 3D data set $[S(\boldsymbol{Q})]_{\rm el}$ taken at 0.7 K for the QSL sample with $x = -0.007$. The image contrast of this $[S(\boldsymbol{Q})]_{\rm el}$ becomes much lower than that of 0.1 K. Only a slight trace of the $\boldsymbol{q} = (\frac{1}{2}, \frac{1}{2}, \frac{1}{2})$ SRO is seen. On the other hand, quite intriguingly, the pinch-point structure around $\boldsymbol{Q} = (1, 1, 1)$ becomes clearer and bears a resemblance to that observed for the spin ice compound $Ho_2Ti_2O_7$ [6,50]. This agrees with our proposal [28] that the magnetic part of the pseudospin-$\frac{1}{2}$ Hamiltonian of TTO is that of dipolar spin ice [46].

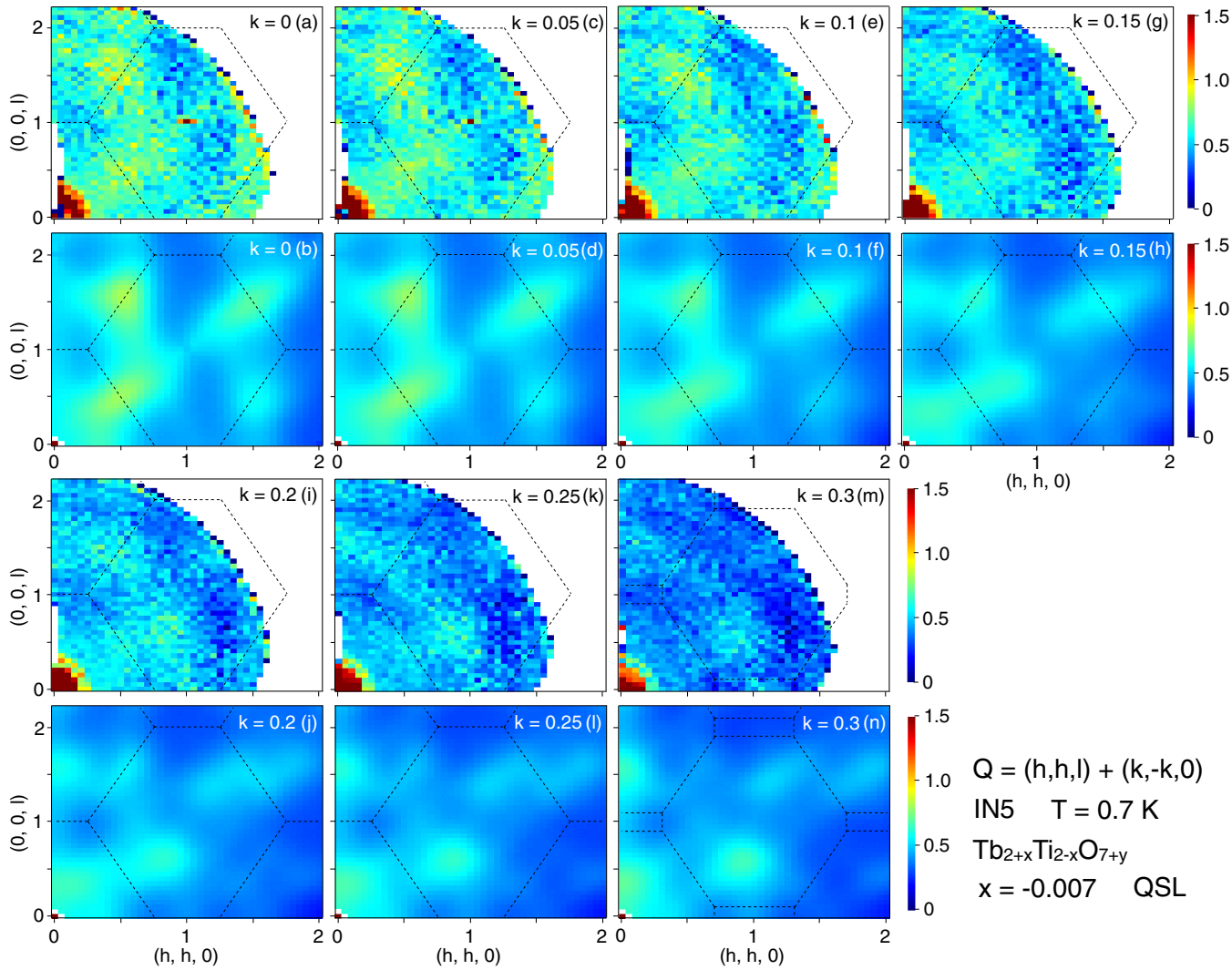

FIG. 4. Intensity maps of 3D data $[S(\boldsymbol{Q})]_{\rm el}$ taken at 0.7 K for the QSL sample with $x = -0.007$. The 3D data are viewed by (a), (c), (e), (g), (i), (k), and (m) 2D slices, which are parallel cross sections of $\boldsymbol{Q} = (h, h, l) + (k, -k, 0)$ with fixed k. These can be compared to (b), (d), (f), (h), (j), (l), and (n) the typical RPA $[S(\boldsymbol{Q})]_{\rm el}$ obtained by least-squares fit using the nine coupling constants, $J_1, \ldots, J_9$, listed in Table I. Dashed lines in these 2D slices in (a)–(n) are boundaries of Brillouin zones.

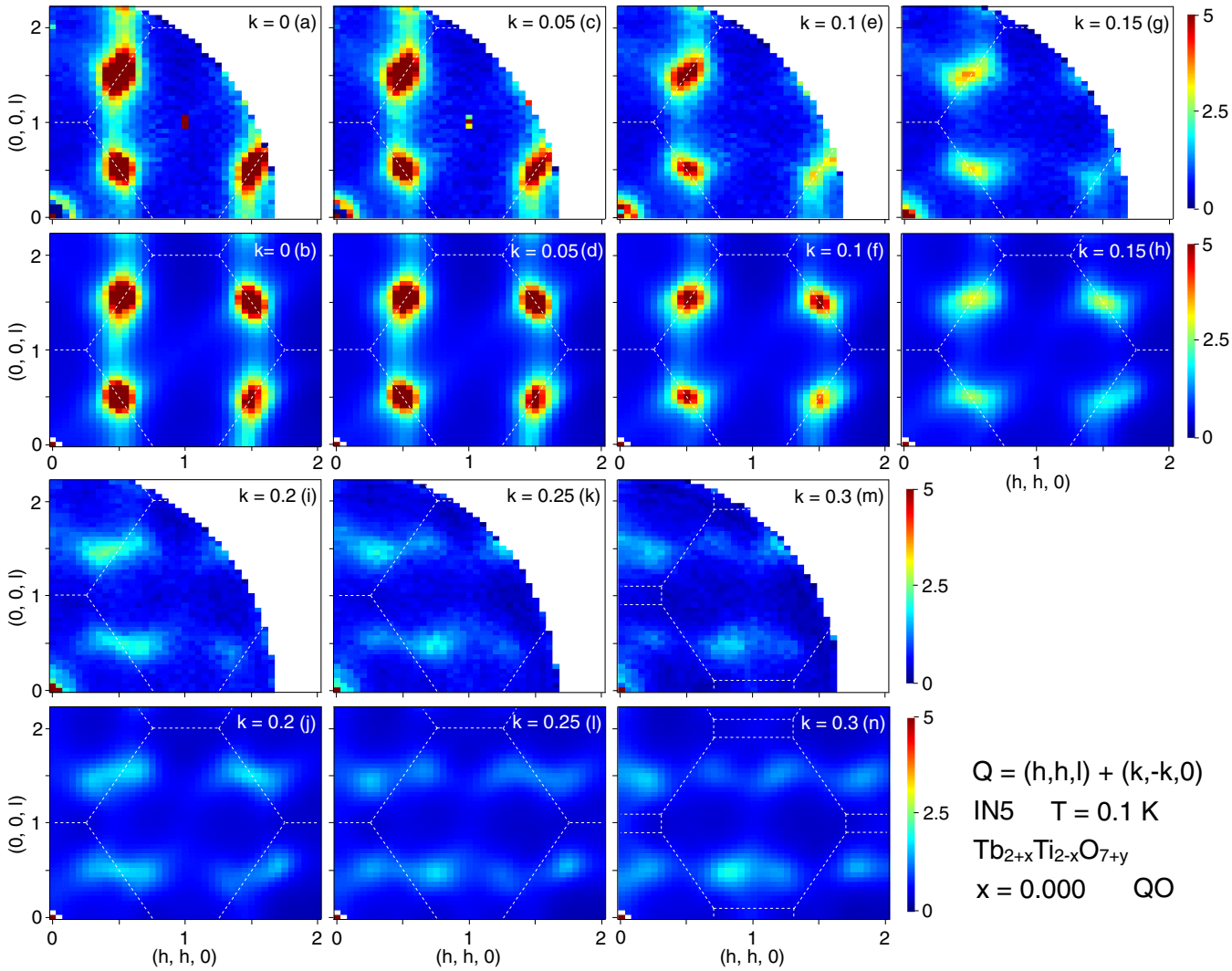

FIG. 5. Intensity maps of 3D data $[S(\boldsymbol{Q})]_{\rm el}$ taken at 0.1 K for the QO sample with $x = 0.000$. The 3D data are viewed by (a), (c), (e), (g), (i), (k), and (m) 2D slices, which are parallel cross sections of $\boldsymbol{Q} = (h, h, l) + (k, -k, 0)$ with fixed k. These can be compared to (b), (d), (f), (h), (j), (l), and (n) the typical RPA $[S(\boldsymbol{Q})]_{\rm el}$ obtained by least-squares fit using the 13 coupling constants, $J_1, \ldots, J_{13}$, listed in Table I. Dashed lines in these 2D slices in (a)–(n) are boundaries of Brillouin zones.

We performed least-squares fits of the observed 3D data set $[S(\boldsymbol{Q})]_{\rm el}$ to the RPA intensity [Eq. (3)] in the same way as those of 0.1 K. In Fig. 3(b) we plot minimized values of χ^2 as a function of the fixed J_1. Figure 3(b) shows that as J_1 is decreased in the range $J_1 < -5D/3$, the fits become unsatisfactory and that the inclusion of further coupling constants J_m with $m_{\rm max} \geqslant 10$ does not improve the fitting. By inspecting several calculated $[S(\boldsymbol{Q})]_{\rm el}$, we chose a typical good result of the fitting. This typical $[S(\boldsymbol{Q})]_{\rm el}$ is shown in Figs. 4(b), 4(d) 4(f), 4(h), 4(j), 4(l), and 4(n), which is calculated using the values of $J_1, \ldots, J_9$ listed in Table I. Considering the lower image contrast and larger statistical errors, the agreement is acceptably good. In fact, both the weakly peaked structures with $\boldsymbol{q} = (\frac{1}{2}, \frac{1}{2}, \frac{1}{2})$ and the pinch-point structure around $\boldsymbol{Q} = (1, 1, 1)$ are reproduced in the RPA $[S(\boldsymbol{Q})]_{\rm el}$. It should be noted that the typical coupling constants listed in the first (0.1 K) and second (0.7 K) rows in Table I are considerably different. This strong temperature dependence also suggests that the fitted values of the coupling constants are either renormalized values or experimental parameters. We also note that at 0.7 K the largest J_m is $J_1 = 1.0$ K, which favors the spin ice state and agrees with our estimation of $J_{\rm nn}$ $(= J_1)$ based on high-temperature susceptibility $(T > 5$ K) [28], which may possibly support the interpretation that J_m are renormalized at low temperatures.

B. QO sample with $x = 0.000$

We show 3D data sets $[S(\boldsymbol{Q})]_{\rm el}$ for the QO sample with $x = 0.000$ taken at 0.1 and 0.7 K in Figs. 5(a), 5(c) 5(e), 5(g), 5(i), 5(k), and 5(m) and 6(a), 6(c) 6(e), 6(g), 6(i), 6(k), and 6(m), respectively. By comparing these figures with the corresponding $[S(\boldsymbol{Q})]_{\rm el}$ shown in Figs. 1 and 4 for the QSL sample, one can see that the 3D data $[S(\boldsymbol{Q})]_{\rm el}$ of these QSL and QO samples show many similarities, which suggests a common origin. This is in stark contrast to the difference in their inelastic spectra shown in Fig. 2 of Ref. [23]. Close inspection of the 3D data $[S(\boldsymbol{Q})]_{\rm el}$ in Figs. 5 and 1 shows that

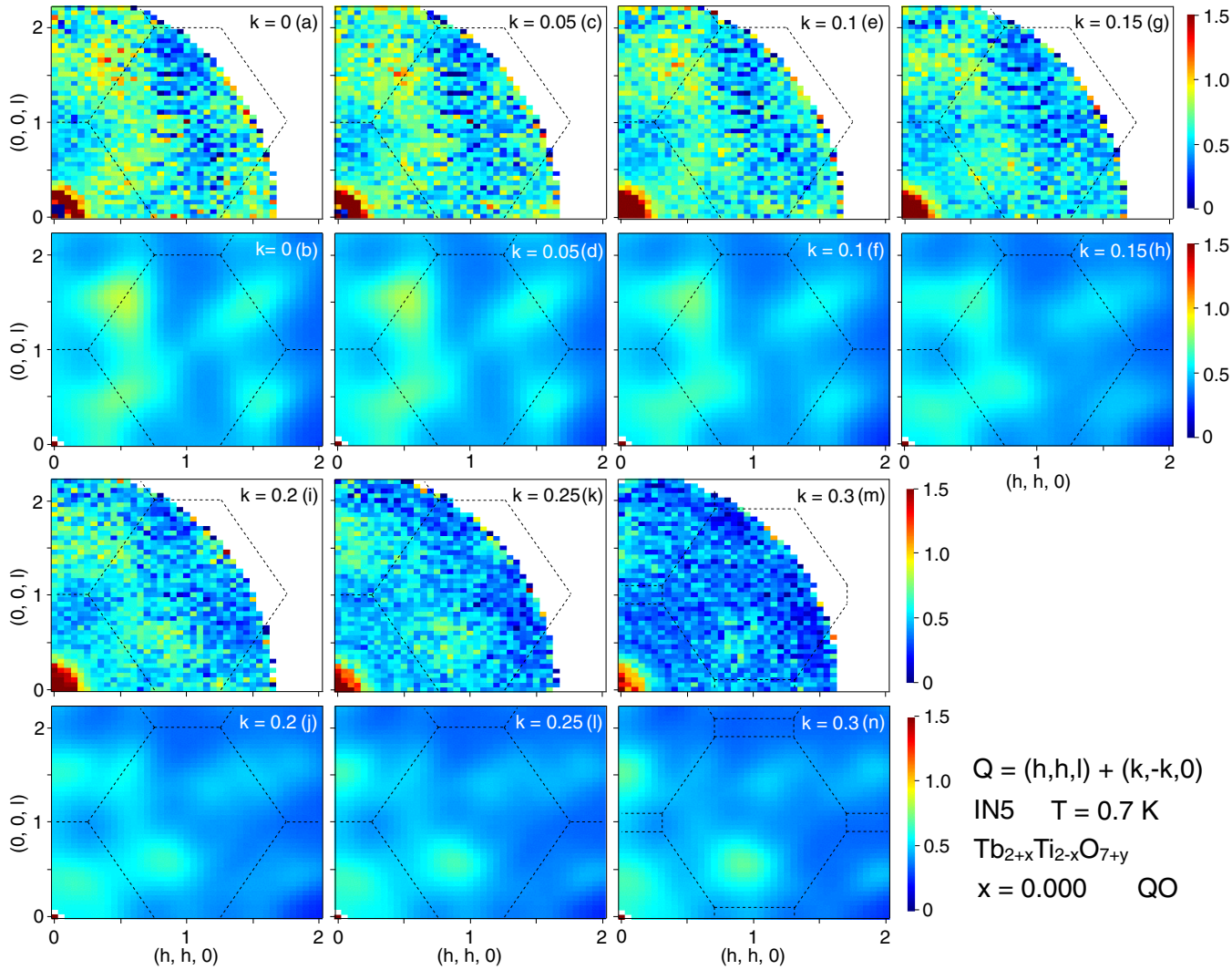

FIG. 6. Intensity maps of 3D data $[S(\boldsymbol{Q})]_{\rm el}$ taken at 0.7 K for the QO sample with $x = 0.000$. The 3D data are viewed by (a), (c), (e), (g), (i), (k), and (m) 2D slices, which are parallel cross sections of $\boldsymbol{Q} = (h, h, l) + (k, -k, 0)$ with fixed k. These can be compared to (b), (d), (f), (h), (j), (l), and (n) the typical RPA $[S(\boldsymbol{Q})]_{\rm el}$ obtained by least-squares fit using the nine coupling constants, $J_1, \ldots, J_9$, listed in Table I. Dashed lines in these 2D slices in (a)–(n) are boundaries of Brillouin zones.

the peaked structures at $\boldsymbol{Q} = (\frac{1}{2}, \frac{1}{2}, \frac{1}{2})$ and $(\frac{1}{2}, \frac{1}{2}, \frac{3}{2})$ of the QO sample are slightly broader than those of the QSL sample and that the peak width of the QO sample is slightly larger than the QSL sample. This indicates that the small quadrupole order slightly suppresses the $\boldsymbol{q} = (\frac{1}{2}, \frac{1}{2}, \frac{1}{2})$ SRO.

We performed least-squares fits of the observed 3D data sets $[S(\boldsymbol{Q})]_{\rm el}$ to the RPA intensity Eq. (3) in the same way as those of the QSL sample. The resulting minimized values of χ^2 are plotted as a function of the fixed J_1 in Figs. 7(a) and 7(b) for the 0.1 and 0.7 K data, respectively. Figures 7(a) and 7(b) and 3(a) and 3(b) show that the least-squares fits provided results parallel to those of the QSL sample. In fact, the typical coupling constants obtained by the fits, which are listed in Table I, have many similarities for the two samples at both 0.1 and 0.7 K. Using these typical J_m listed in Table I, we calculated RPA $[S(\boldsymbol{Q})]_{\rm el}$ and show them in Figs. 5(b), 5(d) 5(f), 5(h), 5(j), 5(l), and 5(n) and 6(b), 6(d) 6(f), 6(h), 6(j), 6(l), and 6(n). The observed and calculated $[S(\boldsymbol{Q})]_{\rm el}$ agree excellently and acceptably well at 0.1 and 0.7 K, respectively.

C. QO sample with $x = 0.003$

Figures 8(a), 8(c) 8(e), 8(g), 8(i), 8(k), 8(m), 8(o), and 8(q) show a 3D data set $[S(\boldsymbol{Q})]_{\rm el}$ taken at 0.1 K for the QO sample with $x = 0.003$. These 3D data are substantially different from those of the QSL sample and the QO sample with $x = 0.000$. The pinch-point structure disappears. The $\boldsymbol{q} = (\frac{1}{2}, \frac{1}{2}, \frac{1}{2})$ SRO becomes much broader than that of the QO sample with $x = 0.000$. Another new point of this sample is that a tiny magnetic Bragg reflection appears at $\boldsymbol{Q} = (\frac{1}{2}, \frac{1}{2}, \frac{3}{2})$. A Q scan through this reflection is plotted in Fig. 8(s), which shows that it disappears at 0.4 K. We note that detector gaps of AMATERAS prohibited us from measuring $\boldsymbol{Q} = (\frac{1}{2}, \frac{1}{2}, \frac{1}{2})$ and (0,0,2) reflections.

The appearance of tiny magnetic Bragg reflections at $\boldsymbol{Q} = (\frac{1}{2}, \frac{1}{2}, \frac{3}{2})$, $(\frac{1}{2}, \frac{1}{2}, \frac{1}{2})$, and (0,0,2) was reported only for samples with large quadrupole orders [26,28,38]. In order to complement our previous experimental data for the magnetic Bragg reflections shown in Fig. 5 of Ref. [26], we show the temperature dependence of the intensities of the Bragg

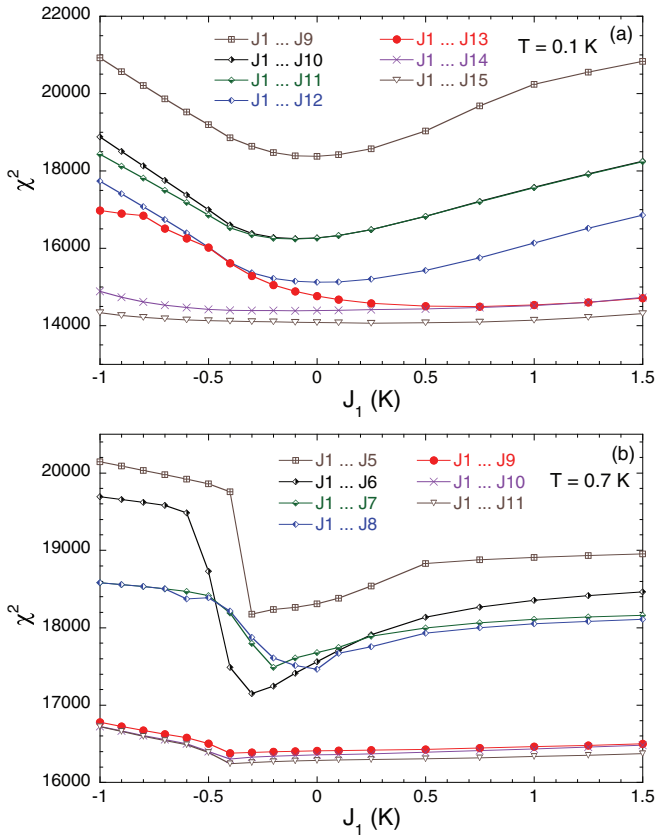

FIG. 7. Minimized values of the weighted sum of squared residuals χ^2 as a function of the fixed parameter J_1. (a) Results of least-squares fits of $[S(\boldsymbol{Q})]_{\rm el}$ with adjustable parameters J_m ($m \leqslant m_{\rm max} = 9, \ldots, 15$) for the QO sample with $x = 0.000$ taken at 0.1 K (Fig. 5). The number of fit data is 11 418. (b) Results of least-squares fits of $[S(\boldsymbol{Q})]_{\rm el}$ with adjustable parameters J_m ($m \leqslant m_{\rm max} = 5, \ldots, 11$) for the QO sample with $x = 0.000$ taken at 0.7 K (Fig. 6). The number of fit data is 10 520.

reflections at $\boldsymbol{Q} = (\frac{1}{2}, \frac{1}{2}, \frac{1}{2})$ and (0,0,2) in Fig. 9. Although statistical errors are large, one can see that the temperature dependence agrees with that shown in Fig. 3 of Ref. [28]. Since several observations of the magnetic Bragg reflections have been accumulated, one may now have to accept the conclusion that the tiny magnetic Bragg reflections, indicating LRO of magnetic moments of the order of $\sim 0.1 \mu_{\rm B}$, have a common origin attributed to the quadrupole LRO. They may possibly be caused by multispin interactions [51,52], which couple the magnetic and quadrupole moments.

We performed least-squares fits of the 3D data set $[S(\boldsymbol{Q})]_{\rm el}$ to the RPA intensity [Eq. (3)] in the same way as for the QSL sample. In Fig. 10 we plot minimized values of χ^2 as a function of the fixed J_1. Figure 10 shows that as J_1 is decreased in the range $J_1 < -5D/3$, the fits become unsatisfactory and that the inclusion of further coupling constants J_m with $m_{\rm max} \geqslant 15$ does not improve the fitting. By inspecting several calculated $[S(\boldsymbol{Q})]_{\rm el}$, we chose a typical good result of the fitting. This typical $[S(\boldsymbol{Q})]_{\rm el}$ is shown in Figs. 8(b), 8(d) 8(f), 8(h), 8(j), 8(l), 8(n), 8(p), and 8(r), which is calculated using the values of $J_1, \ldots, J_{14}$ listed in Table I. One can see that the agreement between the calculated and observed $[S(\boldsymbol{Q})]_{\rm el}$ is not as good as that of the QSL sample. This less satisfactory agreement suggests that the quadrupole order breaks the space group symmetry. In fact, the proposed quadrupole order in Ref. [28] breaks this symmetry. We note that the typical coupling constants obtained by the fitting (Table I) are substantially different from those of the QSL sample.

Figure 11 shows the temperature dependence of the 2D intensity map in the plane $\boldsymbol{Q} = (h, h, l)$ observed in a temperature range $0.2 \leqslant T \leqslant 0.6$ K. Although the $\boldsymbol{Q}$ range and statistical errors are limited, these 2D maps show that the $\boldsymbol{q} = (\frac{1}{2}, \frac{1}{2}, \frac{1}{2})$ SRO disappears already at 0.2 K. The pinch-point structure around (1,1,1), which is similar to that of the QSL sample at 0.7 K, is barely observable in the 0.3 and 0.4 K data. In the temperature range above 0.5 K, where the electric quadrupole order disappears, another kind of spin correlation seems to develop.

IV. DISCUSSION

The question of what $[S(\boldsymbol{Q})]_{\rm el}$ measures is a little difficult to answer correctly. By the present definition, the (nominally) elastic scattering intensity $[S(\boldsymbol{Q})]_{\rm el} = \int_{-\epsilon}^{\epsilon} S(\boldsymbol{Q}, E) dE$ is defined on the basis of the present experimental conditions; therefore, $[S(\boldsymbol{Q})]_{\rm el}$ is different from theoretically elastic scattering. For the sake of simplicity as well as for our interest in the QSL state, we would like to discuss $[S(\boldsymbol{Q})]_{\rm el}$ at the lowest temperature of the present experiments ($T = 0.1$ K). Considering that this temperature scale is approximately equal to the instrumental energy resolution scales, $[S(\boldsymbol{Q})]_{\rm el}$ at 0.1 K is essentially (and roughly) expressed by

$$\sum_{|E_i - E_{\rm G}|, |E_j - E_{\rm G}| < 0.1{\rm K}} \frac{e^{-\beta E_i}}{Z} \left| \langle j | \sum_{\boldsymbol{r}} \sigma_{\boldsymbol{r}}^z e^{i \boldsymbol{Q} \cdot \boldsymbol{r}} | i \rangle \right|^2, \qquad (5)$$

where $E_{\rm G}$ denotes the ground-state energy and the summation runs over low-energy states, $|i\rangle$ and $|j\rangle$.

In previous analyses of the $\boldsymbol{q} = (\frac{1}{2}, \frac{1}{2}, \frac{1}{2})$ SRO [37,38], a few static Ising-spin clusters were assumed to exist, where certain disorders suppressing LRO are also assumed implicitly. These assumptions would be justified if the system behaved within the classical spin paradigm, where states $|i\rangle$ and $|j\rangle$ in Eq. (5) are expressed simply by single states described by the Ising-spin clusters. However, when quantum effects are included, the simple low-energy states would be replaced by linear combinations of the Ising-spin-cluster states. As the number of Ising-spin-cluster states in a linear combination is increased, the system departs from the classical spin paradigm, and consequently, the cluster analyses [37,38] will not work properly. We speculate that the failures to obtain sufficient goodness of fit in Refs. [37,38] indicate that this really happened. For the present RPA analyses, although RPA takes into account quantum effects to a certain extent, RPA is basically a classical approach, and therefore, the same problem would occur, especially when quantum effects become substantially large, e.g., QSL states. We speculate that the breakdown of the classical paradigm is manifested as the necessity of the unexpectedly large number of coupling constants in the present RPA fitting.

The observed $[S(\boldsymbol{Q})]_{\rm el}$ shown in Fig. 1 can be excellently reproduced by the RPA formulas [Eqs. (2) and (3)]. We

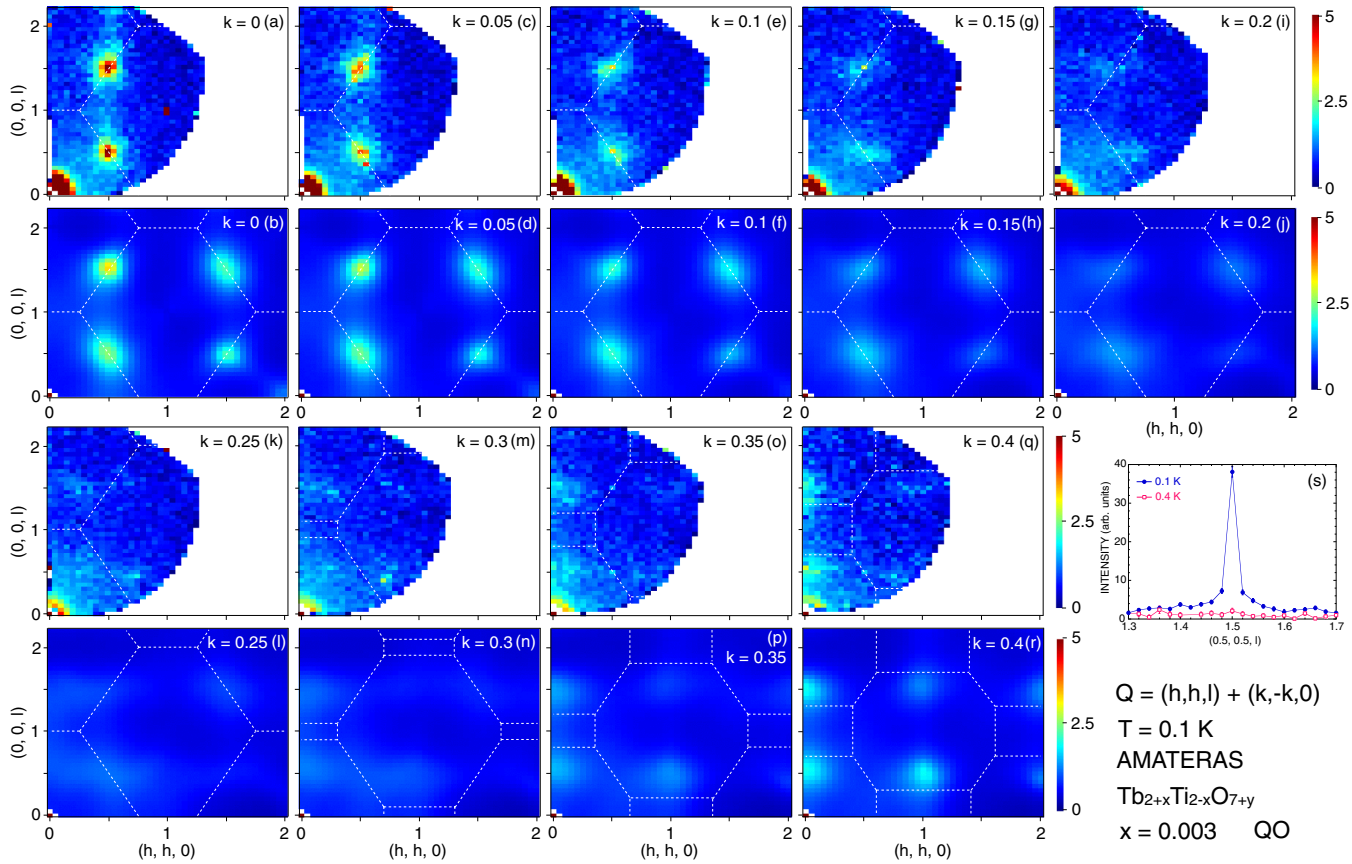

FIG. 8. Intensity maps of 3D data $[S(\boldsymbol{Q})]_{\rm el}$ taken at 0.1 K for the QO sample with $x = 0.003$. The 3D data are viewed by (a), (c), (e), (g), (i), (k), (m), (o), and (q) 2D slices, which are parallel cross sections of $\boldsymbol{Q} = (h, h, l) + (k, -k, 0)$ with fixed k. These can be compared to (b), (d), (f), (h), (j), (l), (n), (p), and (r) the typical RPA $[S(\boldsymbol{Q})]_{\rm el}$ obtained by least-squares fit using the 14 coupling constants, $J_1, \ldots, J_{14}$, listed in Table I. Dashed lines in these 2D slices in (a)–(r) are boundaries of Brillouin zones. (s) Q scan along $\boldsymbol{Q} = (\frac{1}{2}, \frac{1}{2}, l)$ close to magnetic reflection $(\frac{1}{2}, \frac{1}{2}, \frac{3}{2})$.

think that there are two reasons for this successful fit. First, the RPA formulas act as an inverse Fourier transform. The many coupling constants imply that many inverse Fourier components are needed to reproduce the observed $[S(\boldsymbol{Q})]_{\rm el}$. For example, the terms related to J_3 (> 0) in Eq. (2) give rise to higher $[S(\boldsymbol{Q})]_{\rm el}$ at wave vectors $\boldsymbol{Q} = (\frac{1}{2}, \frac{1}{2}, \frac{1}{2})$, $(\frac{1}{2}, \frac{1}{2}, \frac{3}{2})$, etc. Second, the coupling constants J_m in Eq. (1) are allowed by the space group symmetry. As a consequence, the RPA

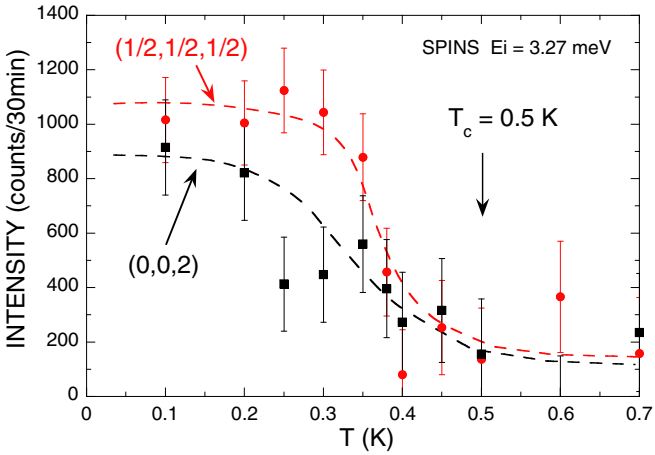

FIG. 9. Temperature dependence of the intensity of Bragg reflection of the powder sample with $x = 0.005$ used in Ref. [26]. These data were measured on the triple-axis spectrometer SPINS operated with $\lambda = 5$ Å at NIST. Error bars represent one standard deviation.

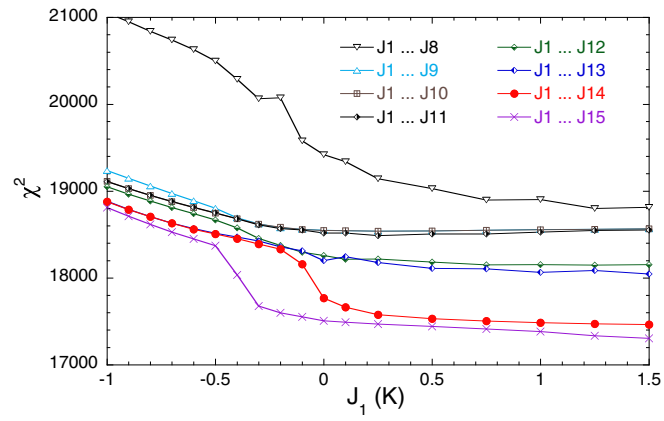

FIG. 10. Minimized values of the weighted sum of squared residuals χ^2 are plotted as a function of the fixed parameter J_1. These are obtained by least-squares fits of $[S(\boldsymbol{Q})]_{\rm el}$ with adjustable parameters J_m ($m \leqslant m_{\rm max} = 8, \ldots, 15$) for the QO sample with $x = 0.003$ taken at 0.1 K (Fig. 8). The number of fit data is 10 570.

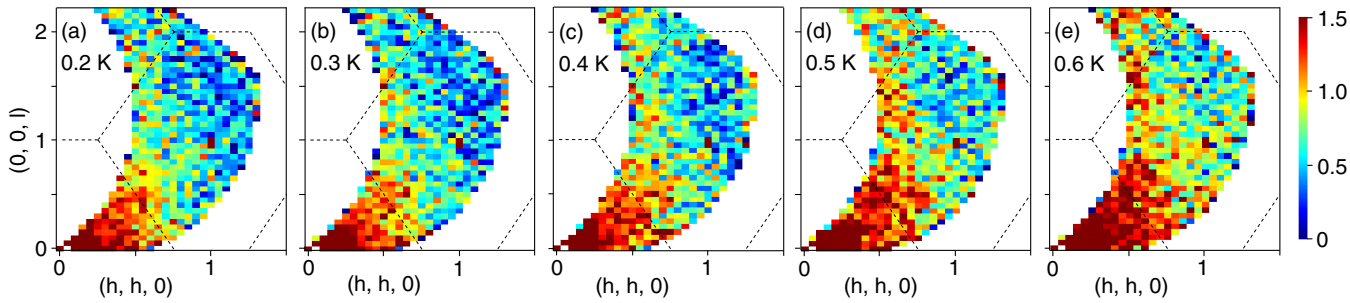

FIG. 11. Temperature dependence of $[S(\boldsymbol{Q})]_{\rm el}$ in the (h, h, l) plane, where $k = 0$ is fixed, for the QO sample with $x = 0.003$. Dashed lines are boundaries of Brillouin zones.

intensity formulas reflect the symmetry of the pyrochlore structure. In this sense, we may conclude that the QSL state of TTO retains the space group symmetry.

Apart from the analyses, one can obtain a few hints for further investigations of the QSL state of TTO directly from a few experimental facts. As discussed in Sec. III A, the 3D data set $[S(\boldsymbol{Q})]_{\rm el}$ at 0.7 K (Fig. 4) shows the pinch-point structure around $\boldsymbol{Q} = (1, 1, 1)$. This suggests that the QSI state proposed in Ref. [24] is somehow continuously connected to the QSL state of TTO. The tiny magnetic Bragg reflections observed in several QO samples, discussed in Sec. III C, are now regarded as an experimental fact. Thus, the pseudospin-$\frac{1}{2}$ Hamiltonian will have to be modified to include coupling between magnetic and quadrupole moments.

V. CONCLUSIONS

Spin correlations of the frustrated pyrochlore oxide $Tb_{2+x}Ti_{2-x}O_{7+y}$ have been investigated by inelastic neutron scattering using single-crystalline samples showing both the quantum-spin-liquid and quadrupole-ordered states. The observed spin correlations show pinch-point type structures around Γ points, an antiferromagnetic short-range order around L points, and tiny antiferromagnetic Bragg scattering at L and Γ points. The $\boldsymbol{q} = (\frac{1}{2}, \frac{1}{2}, \frac{1}{2})$ short-range order was analyzed using a model calculation of a random-phase approximation assuming two-spin interactions among Ising spins. Analyses have shown that the RPA scattering intensity well reproduces the experimental data using temperature- and x-dependent coupling constants of up to tenth-neighbor site pairs. The unexpectedly large number of coupling constants required in the fitting suggest a breakdown of the classical spin paradigm at low temperatures and the necessity of a quantum spin paradigm.

ACKNOWLEDGMENTS

This work was supported by JSPS KAKENHI Grant No. JP25400345. The neutron scattering performed using ILL IN5 (France) was transferred from JRR-3M HER (proposal 11567, 15545) with the approval of ISSP, University of Tokyo, and JAEA, Tokai, Japan. The neutron scattering experiments at J-PARC AMATERAS were carried out under research project No. 2016A0327. The computation was performed on the CX400 supercomputer at the Information Technology Center, Nagoya University.

APPENDIX A: RPA MODEL CALCULATION AND DEFINITIONS

Methods of the RPA model calculation and related definitions are summarized in this section. The effective pseudospin-$\frac{1}{2}$ operators $\sigma^z_{\boldsymbol{r}}$ reside on the pyrochlore lattice sites $\boldsymbol{r} = \boldsymbol{t}_n + \boldsymbol{d}_\nu$, where $\boldsymbol{t}_n$ are fcc translation vectors and $\boldsymbol{d}_\nu$ are four crystallographic sites in the unit cell. These sites and their symmetry axes $\boldsymbol{x}_\nu$, $\boldsymbol{y}_\nu$, and $\boldsymbol{z}_\nu$ [40] are listed in Table II. Representative site pairs $\langle \boldsymbol{r}, \boldsymbol{r}' \rangle_m$ of the coupling constants J_m in Eq. (1) are listed in Table III.

The generalized susceptibility $\chi_{\nu'',\nu'}(\boldsymbol{k}, E)$, where $\boldsymbol{k}$ is a vector in the fcc first Brillouin zone, is computed by solving an RPA equation [39],

$$\sum_{\nu''} \left[\delta_{\nu,\nu''} - \sum_{\nu'''} \chi^0_{\nu,\nu'''}(E) J_{\nu''',\nu''}(\boldsymbol{k}) \right] \chi_{\nu'',\nu'}(\boldsymbol{k}, E) = \chi^0_{\nu,\nu'}(E), \tag{A1}$$

where $J_{\nu,\nu'}(\boldsymbol{k})$ denotes the Fourier transform of the magnetic coupling constants $J_{n,\nu;n',\nu'}$ between sites $\boldsymbol{t}_{n'} + \boldsymbol{d}_{\nu'}$ and $\boldsymbol{t}_n + \boldsymbol{d}_\nu$,

$$J_{\nu,\nu'}(\boldsymbol{k}) = \sum_n J_{n,\nu;n',\nu'} e^{i\boldsymbol{k}\cdot[(\boldsymbol{t}_n + \boldsymbol{d}_\nu) - (\boldsymbol{t}_{n'} + \boldsymbol{d}_{\nu'})]}, \tag{A2}$$

and $\chi^0_{\nu,\nu'}(E)$ is the single-site susceptibility. In the paramagnetic phase

$$\chi^0_{\nu,\nu'}(E) = \delta_{\nu,\nu'} \chi_{\rm L} \frac{\Gamma_0}{\Gamma_0 - iE}, \tag{A3}$$

where $\chi_{\rm L} = 1/(4k_{\rm B}T)$ is the local susceptibility [39] and Γ_0 is a small positive constant.

TABLE II. Four crystallographic sites $\boldsymbol{d}_\nu$ ($\nu = 0, 1, 2, 3$) and their local symmetry axes $\boldsymbol{x}_\nu$, $\boldsymbol{y}_\nu$, and $\boldsymbol{z}_\nu$ [40].

ν	$\boldsymbol{d}_\nu$	$\boldsymbol{x}_\nu$	$\boldsymbol{y}_\nu$	$\boldsymbol{z}_\nu$
0	$\frac{1}{4}(0, 0, 0)$	$\frac{1}{\sqrt{6}}(1, 1, -2)$	$\frac{1}{\sqrt{2}}(-1, 1, 0)$	$\frac{1}{\sqrt{3}}(1, 1, 1)$
1	$\frac{1}{4}(0, 1, 1)$	$\frac{1}{\sqrt{6}}(1, -1, 2)$	$\frac{1}{\sqrt{2}}(-1, -1, 0)$	$\frac{1}{\sqrt{3}}(1, -1, -1)$
2	$\frac{1}{4}(1, 0, 1)$	$\frac{1}{\sqrt{6}}(-1, 1, 2)$	$\frac{1}{\sqrt{2}}(1, 1, 0)$	$\frac{1}{\sqrt{3}}(-1, 1, -1)$
3	$\frac{1}{4}(1, 1, 0)$	$\frac{1}{\sqrt{6}}(-1, -1, -2)$	$\frac{1}{\sqrt{2}}(1, -1, 0)$	$\frac{1}{\sqrt{3}}(-1, -1, 1)$

TABLE III. Representative site pairs $\langle \boldsymbol{r}, \boldsymbol{r}' \rangle_m = \langle \boldsymbol{t}_n + \boldsymbol{d}_\nu, \boldsymbol{t}_{n'} + \boldsymbol{d}_{\nu'} \rangle_m$ of the coupling constants J_m from Eq. (1) are listed using (ν, ν') and $\boldsymbol{r}' - \boldsymbol{r}$. Distances between the site pairs $|\boldsymbol{r}' - \boldsymbol{r}|$ show that the constants J_m in this list are up to 11th-neighbor coupling and that for 3rd-, 7th-, 9th-, and 10th-neighbor site pairs, there are two, two, three, and two nonequivalent site pairs, respectively.

J_m	(ν, ν')	$\boldsymbol{r}' - \boldsymbol{r}$	$\lvert\boldsymbol{r}' - \boldsymbol{r}\rvert$
J_1	(0,1)	(0, 1/4, 1/4)	0.35355
J_2	(0,1)	(1/2, 1/4, −1/4)	0.61237
J_3	(0,0)	(1/2, 1/2, 0)	0.70710
J_4	(0,0)	(1/2, −1/2, 0)	0.70710
J_5	(0,1)	(0, 3/4, −1/4)	0.79057
J_6	(0,1)	(1/2, 1/4, 3/4)	0.93541
J_7	(0,0)	(1, 0, 0)	1
J_8	(0,1)	(1, 1/4, 1/4)	1.06066
J_9	(0,1)	(0, 3/4, 3/4)	1.06066
J_{10}	(0,1)	(1/2, 3/4, −3/4)	1.17260
J_{11}	(0,0)	(1, −1/2, −1/2)	1.224745
J_{12}	(0,0)	(1, 1/2, −1/2)	1.224745
J_{13}	(0,0)	(1, 1/2, 1/2)	1.224745
J_{14}	(0,1)	(0, 5/4, 1/4)	1.274755
J_{15}	(0,1)	(1, 3/4, −1/4)	1.274755
J_{16}	(0,1)	(1/2, 5/4, −1/4)	1.36930

The neutron magnetic scattering intensity $S(\boldsymbol{Q} = \boldsymbol{G} + \boldsymbol{k}, E)$, where $\boldsymbol{G}$ is a reciprocal lattice vector, is given by

$$S(\boldsymbol{Q}, E) \propto f(Q)^2 \frac{1}{1 - e^{-\beta E}} \sum_{\rho,\sigma,\nu,\nu'} (\delta_{\rho,\sigma} - \hat{Q}_\rho \hat{Q}_\sigma) \times U^{(\nu)}_{\rho,z} U^{(\nu')}_{\sigma,z} \mathrm{Im}\{\chi_{\nu,\nu'}(\boldsymbol{k}, E) e^{-i\boldsymbol{G}\cdot(\boldsymbol{d}_\nu - \boldsymbol{d}_{\nu'})}\}, \quad \text{(A4)}$$

where $U^{(\nu)}_{\rho,\alpha}$ is the rotation matrix from the local (α) frame defined at sites $\boldsymbol{t}_n + \boldsymbol{d}_\nu$ to the global (ρ) frame [40,53]. In the quasielastic approximation, the elastic scattering intensity $[S(\boldsymbol{Q})]_{\mathrm{el}}$ is given by integrating Eq. (A4) in the small range $|E| < \epsilon$,

$$[S(\boldsymbol{Q})]_{\mathrm{el}} = \int_{-\epsilon}^{\epsilon} S(\boldsymbol{Q}, E) dE \propto f(Q)^2 \sum_{\rho,\sigma,\nu,\nu'} (\delta_{\rho,\sigma} - \hat{Q}_\rho \hat{Q}_\sigma) \times U^{(\nu)}_{\rho,z} U^{(\nu')}_{\sigma,z} \int_{-\epsilon}^{\epsilon} \frac{\mathrm{Im}\{\chi_{\nu,\nu'}(\boldsymbol{k}, E) e^{-i\boldsymbol{G}\cdot(\boldsymbol{d}_\nu - \boldsymbol{d}_{\nu'})}\}}{E} dE$$
$$\propto f(Q)^2 \sum_{\rho,\sigma,\nu,\nu'} (\delta_{\rho,\sigma} - \hat{Q}_\rho \hat{Q}_\sigma) U^{(\nu)}_{\rho,z} U^{(\nu')}_{\sigma,z} \times \chi_{\nu,\nu'}(\boldsymbol{k}, 0) \cos[\boldsymbol{G} \cdot (\boldsymbol{d}_\nu - \boldsymbol{d}_{\nu'})], \quad \text{(A5)}$$

where $\Gamma_0 \ll \epsilon$ is assumed.

APPENDIX B: LEAST-SQUARES FIT

Technical details of the least-squares fits are summarized in this section. The computations of the least-squares fits were performed on the CX400 supercomputer using a nonlinear least-squares program [54] based on the Levenberg-Marquardt algorithm. The difficulty of the present minimization problem of χ^2 [Eq. (4)] is caused by the fact that χ^2 has many local minima in the parameter space. A trivial origin of this difficulty is that infinitesimal changes of $J_{\mathrm{nn,eff}} \to (1 + \epsilon) J_{\mathrm{nn,eff}}$, where $J_{\mathrm{nn,eff}} = J_1 + \frac{3}{5} D$ (> 0) is the effective ferromagnetic NN coupling for small J_m $(m \geqslant 2)$ [46], $J_m \to (1 + \epsilon) J_m$ $(m \geqslant 2)$, and $\chi_{\mathrm{L}} \to (1 - \epsilon)\chi_{\mathrm{L}}$ in Eq. (A1) bring about $[S(\boldsymbol{Q})]_{\mathrm{el}} \to (1 - \epsilon)[S(\boldsymbol{Q})]_{\mathrm{el}}$ [Eq. (A5)] and, consequently, do not change the $\boldsymbol{Q}$ dependence of $[S(\boldsymbol{Q})]_{\mathrm{el}}$. To avoid the (nearly) rank deficiency in the QR decomposition due to this fact, we fixed J_1 in performing the least-squares fits. Indications of the occurrence of this problem can be seen as several ranges of $\chi^2 \simeq$ const in the curves in Figs. 3, 7, and 10. In addition, there were other unknown origins for the many local minima. These difficulties could be avoided by introducing a weak constraint of the parameters, i.e., adding the penalty function $\sum_{2 \leqslant m \leqslant m_{\max}} \left(\frac{J_m}{1\ \mathrm{K}}\right)^8$ to χ^2. This penalty function weakly restricts J_m in the range $|J_m| < 1$ K, which is a reasonable assumption and can be treated in the framework of the Levenberg-Marquardt algorithm. By inspecting the results of the least-squares fits, we can conclude that sufficiently accurate solutions of the minimization problem were obtained for the present purpose [47]. The uncertainty of the typical coupling constants listed in Table I is of the order of 0.1 K [47].

[1] G. H. Wannier, Phys. Rev. **79**, 357 (1950).
[2] I. Syôzi, Prog. Theor. Phys. **6**, 306 (1951).
[3] Y. Qi, T. Brintlinger, and J. Cumings, Phys. Rev. B **77**, 094418 (2008).
[4] J. S. Gardner, M. J. P. Gingras, and J. E. Greedan, Rev. Mod. Phys. **82**, 53 (2010).
[5] *Introduction to Frustrated Magnetism*, edited by C. Lacroix, P. Mendels, and F. Mila (Springer, Berlin, 2011).
[6] S. T. Bramwell and M. J. P. Gingras, Science **294**, 1495 (2001).
[7] A. P. Ramirez, A. Hayashi, R. J. Cava, R. Siddharthan, and B. S. Shastry, Nature (London) **399**, 333 (1999).
[8] K. Matsuhira, Z. Hiroi, T. Tayama, S. Takagi, and T. Sakakibara, J. Phys. Condens. Matter **14**, L559 (2002).
[9] C. Castelnovo, R. Moessner, and S. L. Sondhi, Nature (London) **451**, 42 (2008).
[10] H. Kadowaki, N. Doi, Y. Aoki, Y. Tabata, T. J. Sato, J. W. Lynn, K. Matsuhira, and Z. Hiroi, J. Phys. Soc. Jpn. **78**, 103706 (2009).
[11] T. Kadowaki and H. Nishimori, Phys. Rev. E **58**, 5355 (1998).
[12] A. D. King, J. Carrasquilla, I. Ozfidan, J. Raymond, E. Andriyash, A. Berkley, M. Reis, T. M. Lanting, R. Harris, G. Poulin-Lamarre, A. Y. Smirnov, C. Rich, F. Altomare, P. Bunyk, J. Whittaker, L. Swenson, E. Hoskinson, Y. Sato, M. Volkmann, E. Ladizinsky, M. Johnson, J. Hilton, and M. H. Amin, Nature (London) **560**, 456 (2018).
[13] L. Savary and L. Balents, Rep. Prog. Phys. **80**, 016502 (2017).
[14] P. W. Anderson, Mater. Res. Bull. **8**, 153 (1973).
[15] K. Hirakawa, H. Kadowaki, and K. Ubukoshi, J. Phys. Soc. Jpn. **54**, 3526 (1985).

[16] J. S. Gardner, S. R. Dunsiger, B. D. Gaulin, M. J. P. Gingras, J. E. Greedan, R. F. Kiefl, M. D. Lumsden, W. A. MacFarlane, N. P. Raju, J. E. Sonier, I. Swainson, and Z. Tun, Phys. Rev. Lett. **82**, 1012 (1999).

[17] T.-H. Han, J. S. Helton, S. Chu, D. G. Nocera, J. A. Rodriguez-Rivera, C. Broholm, and Y. S. Lee, Nature (London) **492**, 406 (2012).

[18] K. A. Ross, L. Savary, B. D. Gaulin, and L. Balents, Phys. Rev. X **1**, 021002 (2011).

[19] L.-J. Chang, S. Onoda, Y. Su, Y.-J. Kao, K.-D. Tsuei, Y. Yasui, K. Kakurai, and M. R. Lees, Nat. Commun. **3**, 992 (2012).

[20] Y. Shen, Y.-D. Li, H. Wo, Y. Li, S. Shen, B. Pan, Q. Wang, H. C. Walker, P. Steffens, M. Boehm, Y. Hao, D. L. Quintero-Castro, L. W. Harriger, M. D. Frontzek, L. Hao, S. Meng, Q. Zhang, G. Chen, and J. Zhao, Nature (London) **540**, 559 (2016).

[21] B. Fåk, S. Bieri, E. Canévet, L. Messio, C. Payen, M. Viaud, C. Guillot-Deudon, C. Darie, J. Ollivier, and P. Mendels, Phys. Rev. B **95**, 060402 (2017).

[22] R. Sibille, N. Gauthier, H. Yan, M. Ciomaga Hatnean, J. Ollivier, B. Winn, U. Filges, G. Balakrishnan, M. Kenzelmann, N. Shannon, and T. Fennell, Nat. Phys. **14**, 711 (2018).

[23] H. Kadowaki, M. Wakita, B. Fåk, J. Ollivier, S. Ohira-Kawamura, K. Nakajima, H. Takatsu, and M. Tamai, J. Phys. Soc. Jpn. **87**, 064704 (2018).

[24] H. R. Molavian, M. J. P. Gingras, and B. Canals, Phys. Rev. Lett. **98**, 157204 (2007).

[25] M. J. P. Gingras and P. A. McClarty, Rep. Prog. Phys. **77**, 056501 (2014).

[26] T. Taniguchi, H. Kadowaki, H. Takatsu, B. Fåk, J. Ollivier, T. Yamazaki, T. J. Sato, H. Yoshizawa, Y. Shimura, T. Sakakibara, T. Hong, K. Goto, L. R. Yaraskavitch, and J. B. Kycia, Phys. Rev. B **87**, 060408 (2013).

[27] M. Wakita, T. Taniguchi, H. Edamoto, H. Takatsu, and H. Kadowaki, J. Phys.: Conf. Ser. **683**, 012023 (2016).

[28] H. Takatsu, S. Onoda, S. Kittaka, A. Kasahara, Y. Kono, T. Sakakibara, Y. Kato, B. Fåk, J. Ollivier, J. W. Lynn, T. Taniguchi, M. Wakita, and H. Kadowaki, Phys. Rev. Lett. **116**, 217201 (2016).

[29] H. Takatsu, T. Taniguchi, S. Kittaka, T. Sakakibara, and H. Kadowaki, J. Phys.: Conf. Ser. **683**, 012022 (2016).

[30] H. Kadowaki, H. Takatsu, and M. Wakita, Phys. Rev. B **98**, 144410 (2018).

[31] S. Onoda and Y. Tanaka, Phys. Rev. B **83**, 094411 (2011).

[32] S. B. Lee, S. Onoda, and L. Balents, Phys. Rev. B **86**, 104412 (2012).

[33] M. Hermele, M. P. A. Fisher, and L. Balents, Phys. Rev. B **69**, 064404 (2004).

[34] Y. Yasui, M. Kanada, M. Ito, H. Harashina, M. Sato, H. Okumura, K. Kakurai, and H. Kadowaki, J. Phys. Soc. Jpn. **71**, 599 (2002).

[35] T. Fennell, M. Kenzelmann, B. Roessli, M. K. Haas, and R. J. Cava, Phys. Rev. Lett. **109**, 017201 (2012).

[36] S. Petit, P. Bonville, J. Robert, C. Decorse, and I. Mirebeau, Phys. Rev. B **86**, 174403 (2012).

[37] K. Fritsch, K. A. Ross, Y. Qiu, J. R. D. Copley, T. Guidi, R. I. Bewley, H. A. Dabkowska, and B. D. Gaulin, Phys. Rev. B **87**, 094410 (2013).

[38] S. Guitteny, I. Mirebeau, P. Dalmas de Réotier, C. V. Colin, P. Bonville, F. Porcher, B. Grenier, C. Decorse, and S. Petit, Phys. Rev. B **92**, 144412 (2015).

[39] J. Jensen and A. R. Mackintosh, *Rare Earth Magnetism* (Clarendon, Oxford, 1991).

[40] H. Kadowaki, H. Takatsu, T. Taniguchi, B. Fåk, and J. Ollivier, SPIN **05**, 1540003 (2015).

[41] H. Takatsu, T. Taniguchi, S. Kittaka, T. Sakakibara, and H. Kadowaki, J. Phys.: Conf. Ser. **828**, 012007 (2017).

[42] Experimental data of the sample with $x = -0.007$ are available at B. Fåk, H. Kadowaki, J. Ollivier, and M. Wakita (2015), Institut Laue-Langevin (ILL), doi:10.5291/ILL-DATA.4-05-628.

[43] Experimental data of the sample with $x = 0.000$ are available at B. Fåk, H. Kadowaki, and J. Ollivier (2016), Institut Laue-Langevin (ILL), doi:10.5291/ILL-DATA.4-05-635.

[44] H. Kadowaki, https://github.com/kadowaki-h/AbsorptionFactorIN5; https://github.com/kadowaki-h/AbsorptionFactorAMATERAS.

[45] R. Ewings, A. Buts, M. Le, J. van Duijn, I. Bustinduy, and T. Perring, Nucl. Instrum. Methods Phys. Res., Sect. A **834**, 132 (2016).

[46] B. C. den Hertog and M. J. P. Gingras, Phys. Rev. Lett. **84**, 3430 (2000).

[47] See Supplemental Material at http://link.aps.org/supplemental/10.1103/PhysRevB.99.014406 for spin correlations of quantum spin liquid and quadrupole-ordered states of $Tb_{2+x}Ti_{2-x}O_{7+y}$.

[48] Q. J. Li, Z. Y. Zhao, C. Fan, F. B. Zhang, H. D. Zhou, X. Zhao, and X. F. Sun, Phys. Rev. B **87**, 214408 (2013).

[49] E. Kermarrec, D. D. Maharaj, J. Gaudet, K. Fritsch, D. Pomaranski, J. B. Kycia, Y. Qiu, J. R. D. Copley, M. M. P. Couchman, A. O. R. Morningstar, H. A. Dabkowska, and B. D. Gaulin, Phys. Rev. B **92**, 245114 (2015).

[50] T. Fennell, P. P. Deen, A. R. Wildes, K. Schmalzl, D. Prabhakaran, A. T. Boothroyd, R. J. Aldus, D. F. McMorrow, and S. T. Bramwell, Science **326**, 415 (2009).

[51] H. R. Molavian, P. A. McClarty, and M. J. P. Gingras, arXiv:0912.2957.

[52] J. G. Rau and M. J. P. Gingras, arXiv:1806.09638.

[53] Y.-J. Kao, M. Enjalran, A. Del Maestro, H. R. Molavian, and M. J. P. Gingras, Phys. Rev. B **68**, 172407 (2003).

[54] H. Kadowaki, https://github.com/kadowaki-h/least65OMP.